Turbulent Flow through Idealized Emergent Vegetation

T. Stoesser, M.ASCE[1]; S. J. Kim[2]; and P. Diplas, M.ASCE[3]

Abstract: This paper presents results of several large-eddy simulations (LES) of turbulent flow in an open channel through staggered arrays of rigid, emergent cylinders, which can be regarded as idealized vegetation. In this study, two cylinder Reynolds numbers, $R_D = 1,340$ and $R_D = 500$, and three vegetation densities are considered. The LES of the lowest density and at $R_D = 1,340$ corresponds to a recently completed laboratory experiment, the data of which is used to validate the simulations. Fairly good agreement between calculated and measured first- and second-order statistics along measurement profiles is found, confirming the accuracy of the simulations. The high resolution of the simulations enables an explicit calculation of drag forces, decomposed into pressure and friction drag, that are exerted on the cylinders. The effect of the cylinder Reynolds number and the cylinder density on the drag and hence on the flow resistance is quantified and in agreement with previous experimental studies. Turbulence structures are visualized through instantaneous pressure fluctuations, isosurfaces of the Q-criterion and contours of vertical vorticity in horizontal planes. Analysis of velocity time signals and distributions of drag and lift forces over time reveals that flow and turbulence are more influenced by the vegetation density than by the cylinder Reynolds number.

DOI: 10.1061/(ASCE)HY.1943-7900.0000153

CE Database subject headings: Vegetation; Turbulent flow; Drag; Flow resistance.

Author keywords: Vegetation; Turbulence; LES; Drag; Flow resistance; Coherent structures.

Introduction

The presence of vegetation in the aquatic environment considerably alters the turbulent flow in streams, rivers, and floodplains. The additional drag exerted by plants largely influences the horizontal and vertical distributions of mean and instantaneous velocity, turbulence quantities, and Reynolds stresses as well as transport of sediments and solutes. Furthermore, the flow through partially vegetated channels or emergent and submerged vegetation is characterized by significant velocity gradients (laterally, longitudinally, and vertically) resulting in shear layer formation between the canopy flow and the flow outside the vegetation. Recent research has focused on deliberately using vegetation on banks and floodplains for attenuating floods, filtering contaminants, promoting water self-purification, sheltering aquatic life, and even changing channel shape (Bennett et al. 2002).

In order to quantify the effects of vegetation in terms of flow resistance, Petryk and Bosmajian (1975) introduced a force-equilibrium approach and postulated that the gravity force is equal to the boundary shear stress and the drag forces induced by the emergent vegetation. The drag force of vegetation can be simplistically calculated using the formula for a single circular cylinder by assuming that vegetation can be idealized as a rigid circular cylinder. A number of experimental studies further refined this approach for different flow conditions (Pasche and Rouve 1985; Wu et al. 1999; Tsihrintzis 2001; Bennett et al. 2002; Stone and Shen 2002; Wilson et al. 2003; Lee et al. 2004; Takemura and Tanaka 2007). In a recent experimental study Tanino and Nepf (2008) evaluated the drag force and the drag coefficient as a function of vegetation density for various, relatively low, cylinder Reynolds numbers ($R_D = 30-700$). A number of experimental studies have focused on detailed examination of the flow field and turbulence structure within a plant canopy. These studies have involved modeling vegetation as an array of rigid cylinders of the same height and diameter at regular spacing (Pasche and Rouve 1985; Tsujimoto and Kitamura 1990; Shimizu and Tsujimoto 1994; Dunn et al. 1996; Nepf 1999) and have observed that the spatially and time-averaged velocity profile within an emergent or submerged vegetated layer (irrespective of whether the vegetation is rigid or flexible) no longer follows the universal logarithmic law. Furthermore, not only the spatially averaged velocity profile is altered considerably but also the vertical distribution of turbulence intensities, Reynolds stresses and kinetic energy exhibit large differences from those of unobstructed channel flow (Nepf 1999; Lopez and Garcia 2001). In a recent study Liu et al. (2008) provided quantitative evidence that the local flow around single vegetation elements is spatially heterogeneous by evaluating turbulence statistics of flow through emergent and submerged vegetation along six different verticals around one vegetation element within an array of elements.

A more complete three-dimensional picture of the flow can be obtained from computational fluid dynamics (CFD) models. The majority of CFD models solve the 3D steady or unsteady Reynolds-averaged–Navier-Stokes (RANS) equations and are capable of accurately predicting the time-averaged flow field. Usually, RANS models are operated on coarser grids and vegetation

[1]Assistant Professor, School of Civil and Environmental Engineering, Georgia Institute of Technology, Atlanta, GA 30332 (corresponding author). E-mail: thorsten@ce.gatech.edu

[2]Ph.D. Student, School of Civil and Environmental Engineering, Georgia Institute of Technology, Atlanta, GA 30332. E-mail: a.sujin.kim@gatech.edu

[3]Professor, Dept. of Civil and Environmental Engineering, Virginia Tech, Blacksburg, VA 24061. E-mail: pdiplas@vt.edu

Note. This manuscript was submitted on August 1, 2009; approved on April 21, 2010; published online on April 26, 2010. Discussion period open until May 1, 2011; separate discussions must be submitted for individual papers. This paper is part of the ***Journal of Hydraulic Engineering***, Vol. 136, No. 12, December 1, 2010. ©ASCE, ISSN 0733-9429/2010/12-1003–1017/$25.00.

drag is accounted for through additional source terms that are added to the momentum and turbulence transport equations. These models are the most practical approaches offering reasonable accuracy for the prediction of the time-averaged flow field (Shimizu and Tsujimoto 1994; Naot et al. 1996; Neary 2000; Fischer-Antze et al. 2001; Choi and Kang 2004). In addition to RANS models require modified turbulence closure models featuring drag-related sink terms in the turbulent transport equations to be able to predict reasonably well the turbulence quantities within the vegetation layer. The source terms of both the momentum and transport equations require a-priori knowledge of the drag coefficient and additional empirical constants. The strength of RANS or unsteady RANS (URANS) models lies in their computational efficiency and their portability to field scale flows. Hence, RANS or URANS models have not been applied to simulate the flow through vegetation with individual plants/cylinders resolved by the numerical grid. This is probably due the fact that standard RANS/URANS models were less successful in predicting the flow and turbulence around single cylinders (Rodi 1997; Luebcke et al. 2001) or the flow in tube bundles (Rollet-Miet et al. 1999; Hanjalic and Hadzic 1998). Both flows are very similar to the flow through an idealized vegetation layer.

Recently, large-eddy simulation (LES) has become a popular research tool to investigate flows in which turbulence structures dominate the flow statistics. LES provides an almost complete description of the instantaneous unsteady 3D turbulent flow field, resolving large-scale unsteadiness and asymmetries (large eddies) resulting from flow instabilities. First, LES results of channel flow through vegetation were presented by Cui and Neary (2002), Stoesser et al. (2006), and Palau et al. (2007) and provided evidence that LES is able to elucidate large-scale coherent structures, their role in vegetative flow resistance, and their contribution to Reynolds stresses and turbulence quantities.

In this paper, we present large-eddy simulations of turbulent channel flow through a matrix of surface protruding circular cylinders, which can be regarded as idealized emergent vegetation. Each cylinder is explicitly resolved through a high resolution bodyfitted grid with the first grid point well within the viscous sublayer of the cylinder. This allows for the direct calculation of acting drag and lift forces. To validate the LES, time-averaged velocities and turbulence intensities are compared with laboratory data at selected profiles. The effects of vegetation density and cylinder Reynolds number on the turbulence statistics and the instantaneous flow field are discussed and analyzed.

Numerical Framework

The LES code (Hydro3D-GT) used in this study is based on the finite volume method on a curvilinear grid with collocated variable arrangement (Stoesser 2002). The Hydro3D-GT code solves the filtered Navier-Stokes equations for incompressible fluid flow (Pope 2000)

$$\frac{\partial u_i}{\partial x_i} = 0 \tag{1}$$

$$\frac{\partial u_i}{\partial t} + \frac{\partial u_i u_j}{\partial x_j} = -\frac{\partial p}{\partial x_j} + \frac{\partial (2\nu S_{ij})}{\partial x_j} - \frac{\partial \tau_{ij}}{\partial x_j} \tag{2}$$

where u_i and u_j (i or j=1, 2, or 3)=resolved velocity vectors (i.e., $u_1=u$, $u_2=v$, and $u_3=w$ denoting the velocity components in x, y, and z axis direction, respectively) and p=resolved pressure divided by the density. These quantities are filtered in space. Similarly, x_i and x_j represent the spatial location vectors in x, y, and z axis direction, respectively, ν=kinematic viscosity, and S_{ij} =filtered strain-rate tensor, defined as $S_{ij}=1/2[(\partial u_i/\partial x_j)+(\partial u_j/\partial x_i)]$. The term τ_{ij} results from the unresolved subgrid scale fluctuations and needs to be modeled by a subgrid scale (SGS) model. The dynamic version of the original Smagorinsky (Smagorinsky 1963) SGS model (Germano et al. 1991) is employed to approximate the anisotropic part of τ_{ij}, i.e., τ_{ij}^a, as $\tau_{ij}^a=\tau_{ij}-(2/3)\delta_{ij}k_r(=-2\nu_t S_{ij})$, where δ_{ij}=Kronecker delta and k_r =residual kinetic energy. Then, an anisotropic filter ($\Delta=(\Delta x\Delta y\Delta z)^{1/3}$) together with the characteristic filtered rate of strain ($|S|=(2S_{ij}S_{ij})^{1/2}$) are used to compute the subgrid scale eddy viscosity ν_t as $\nu_t=(C_s\Delta)^2|S|$. The Smagorinsky constant C_s =calculated locally by making use of the flow information available from the smallest resolved scales. A double filtering procedure leads to a closed expression, commonly referred to as Germano's identity, relating filter stresses at different filter levels to each other. This additional information is then used to determine the model parameter C_s through local averaging.

The convection and diffusion terms in the Navier-Stokes equations are approximated by central differences ensuring second-order accuracy in space. An explicit Adams-Bashforth scheme is used to discretize the equations in time providing second-order accuracy in time.

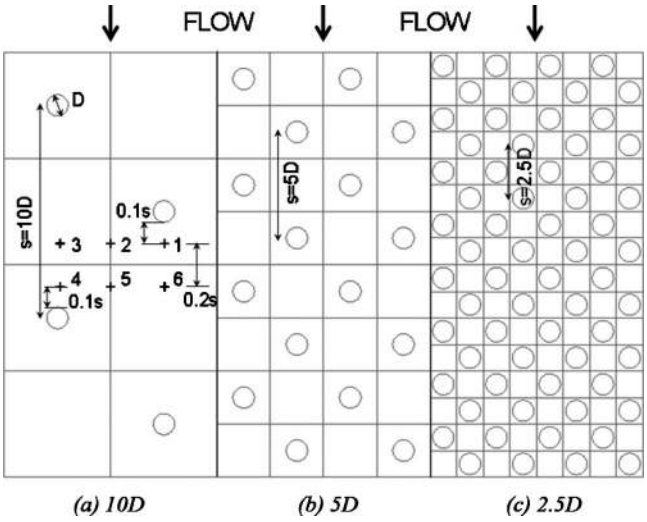

Fig. 1. Flow domain and cylinder arrangement for the three different setups. The measurement locations in the experiment are also depicted.

Simulation Setup

The setup for the first simulation of this study is chosen to match the experiments carried out by Liu et al. (2008) the data of which is used to validate the LES. Liu et al. (2008) placed a matrix of rigid cylinders in a staggered arrangement into a rectangular flume and carried out detailed laser doppler velocimeter (LDV) measurements at the six verticals within the flow as indicated in Fig. 1(a). In Fig. 1, s, is defined as the distance between two cylinders in the streamwise direction and in Liu et al.'s experiment s=10D. The vegetation density φ, here defined as the volume that is occupied by the cylinders over the total volume, is φ=0.0157. The cylinder Reynolds number based on the bulk ve-

J. Hydraul. Eng. 2010.136:1003-1017.

Table 1. Physical Parameters of the Simulations

	10*D* case	5*D* case	2.5*D* case
Number of cylinders in the domain	4	16	64
Cylinder volume fraction, φ	0.0157	0.0628	0.2513
Width fraction factor, ψ	1.11	1.25	1.67

locity, u(bulk) and the cylinder diameter D is $R_D=1,340$. In addition to the 10*D* case of Liu et al. (2008), numerical experiments are carried out for two additional vegetation densities, i.e., $s=5D$ and $s=2.5D$, or $\varphi=0.0628$ and $\varphi=0.2513$, respectively, and at one additional (lower) flow rate which yields $R_D=500$. In total, six different numerical experiments are performed, details for which are found in Table 1. The computational flow domain chosen is the same for all cases and spans 20D in streamwise, 10*D* in spanwise, and 10.22*D* (corresponding to the water depth) in the vertical direction, respectively.

A block-structured grid composed of Cartesian H-grid and curvilinear O-grid blocks is employed and is depicted in Fig. 2. While the Cartesian grid is uniform in the horizontal plane the grid of the O-grid block is stretched toward the cylinder. In the wall-normal direction the grid is stretched from the channel bed to the free surface. The details of each grid of the six numerical experiments are summarized in Table 2.

Boundary Conditions

At the channel bed and at the cylinder wall the no-slip boundary condition is applied. This is justified by the fact that 3–4 points off the wall are situated within the viscous sublayer. Fig. 3 presents the distribution of the dimensionless wall distance $y^+=\Delta y u_*/\nu$ around the cylinder for the three different vegetation densities at $R_D=1,350$. The upper row of Fig. 3 presents contours of y^+ and it can be seen that only locally maximum values of $y^+=7$ prevail. A more quantitative distribution of the dimensionless wall spacing is provided in the lower row of Fig. 3 where y^+ values at three different elevations, i.e., near the bed, at mid depth and near the water surface along the circumference of the cylinder are plotted. This figure provides proof of the validity of using the no-slip condition because in all three cases the wall distance is found to be in the order of $y^+=1$ for most of the circumference. However, toward the point of flow separation, i.e., where the highest velocities tangential to the cylinder wall are found, maximum values of $y^+=4$ in the 10*D* case, $y^+=5$ in the 5*D* case and $y^+=6$ in the 2.5*D* case are observed. Though those values are still below $y^+=11$, i.e., the edge of the viscous sublayer an additional simulation for the 10*D*, $R_D=1,340$ at a considerably finer grid resolution is carried out. This is considered the (worst) case in terms of grid resolution and it can be seen from Fig. 3, that the near wall resolution is approximately two times higher in the finer grid than in the original grid.

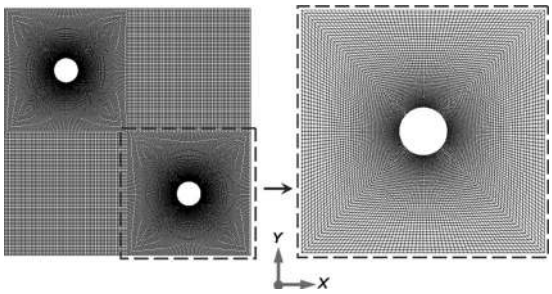

Fig. 2. Part of the employed grid for the 10*D* case showing: (a) block-structured grid composed of *H*- and *O*-grids; (b) stretched *O*-grid for the cylinder region

Periodic boundary conditions are applied in the streamwise and spanwise directions, and the free surface is set as a frictionless rigid lid and is treated as a plane of symmetry. The simulations are initially run for about 20 eddy turn-over time units, t_e, defined as the water depth over the friction velocity, in order to establish fully developed flow conditions. For the calculation of flow and turbulence statistics the simulations are then continued for 50+ eddy turn-over time units. The code uses an adjustable time step size based on the CFL criteria with maximum CFL numbers of 0.5. The code is parallelized using MPI and the maximum number of CPUs employed in this study is 288 for the 2.5*D* case and consumed approximately 110,000 CPUh for approximately 300,000 timesteps.

Results and Discussion

Time-Averaged Flow Field and Turbulence Statistics

Fig. 4 presents the LES calculated time-averaged and normalized (with the bulk velocity) streamwise velocities along six profiles for the three vegetation densities, i.e., 10*D*, 5*D*, and 2.5*D*. Also plotted are the results from the finer grid simulation and the experimental velocity data with which the simulation of the 10*D* case is validated. First of all, differences between original-grid and finer-grid LES are negligibly small, confirming the adequacy of the original grid. The velocity profiles of the 10*D* simulation (black and gray solid lines) match the Liu et al. (2008) observations quite well in particular at Profiles #3, #4, #1, and #6, i.e., along the profiles in front of the cylinder and behind the cylinder (Fig. 1). There is a local acceleration of the flow near the surface just behind the cylinder, i.e., profile #1, which might be the result of a local water-surface depression (the water-surface was not measured in great detail hence this is speculative). The fact that

Table 2. Numerical Parameters of the Simulations

R_D	Spacing, s	Gridpoints in *H*-grid, $n_x\times n_y\times n_z\times n_{set}$	Gridpoints in *O*-grid, $n_\theta\times n_r\times n_z\times n_{set}$	Total number of gridpoints
1,340	10*D*	$82\times82\times122\times4$	$(82\times4)\times52\times122\times4$	11,604,640
	5*D*	$62\times62\times122\times16$	$(62\times4)\times32\times122\times16$	22,994,560
	2.5*D*	$42\times42\times122\times64$	$(42\times4)\times12\times122\times64$	29,514,240
500	10*D*	$62\times62\times122\times4$	$(62\times4)\times47\times122\times4$	7,564,000
	5*D*	$42\times42\times122\times16$	$(42\times4)\times27\times122\times16$	12,297,600
	2.5*D*	$22\times22\times122\times64$	$(22\times4)\times9\times122\times64$	9,963,008

J. Hydraul. Eng. 2010.136:1003-1017.

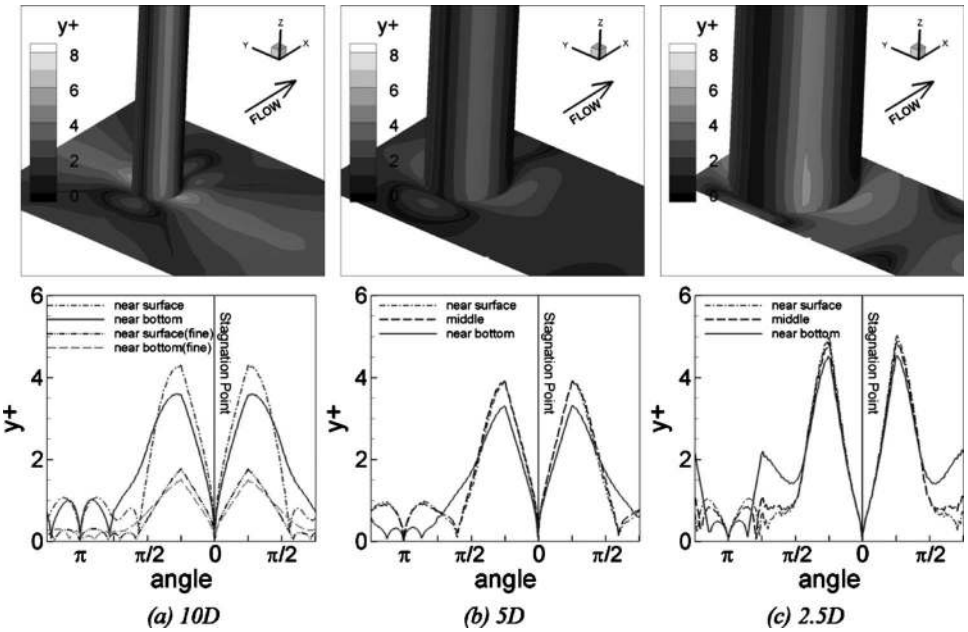

Fig. 3. Contours of the dimensionless wall distance around the cylinder (above) and $y+$ distributions around the cylinder circumference at three selected heights (below). The stagnation point is located at zero.

this feature is not picked up by the LES (using a rigid lid) supports the hypothesis of a local water surface depression. Also, there is a small but consistent overestimation of calculated streamwise velocity magnitude of approximately 7% visible in Profiles #2 and #5. This could be due to an underestimation of u(bulk), or due to the fact that the flow is slightly deeper between cylinders, or both. Noteworthy is a near bed velocity bulge in Verticals #1 and #6 in the 10D case that is accurately predicted by the LES. This velocity bulge is a result of the prevailing secondary flow (discussed below) entraining high momentum fluid into the wake near the bed. This mechanism has been discussed by Liu et al. 2008 as well. Such a distinct velocity bulge is absent or less pronounced, respectively, in the 5D and 2.5D cases. Worth mentioning is the fact that streamwise velocities are found to be almost constant over the depth and vegetation density and that the profiles deviates marginally from a logarithmic distribution irrespective of location.

Fig. 5 compares calculated vertical velocities with measured data along the six verticals for the 10D case but also includes profiles for the other two cases. The agreement between the 10D case simulation and the experiment is quite good, regardless of grid resolution. Overall very small vertical velocities are observed in both 10D and 5D cases except just behind the cylinder (Verticals #1 and #6) where relatively large values of vertical velocity

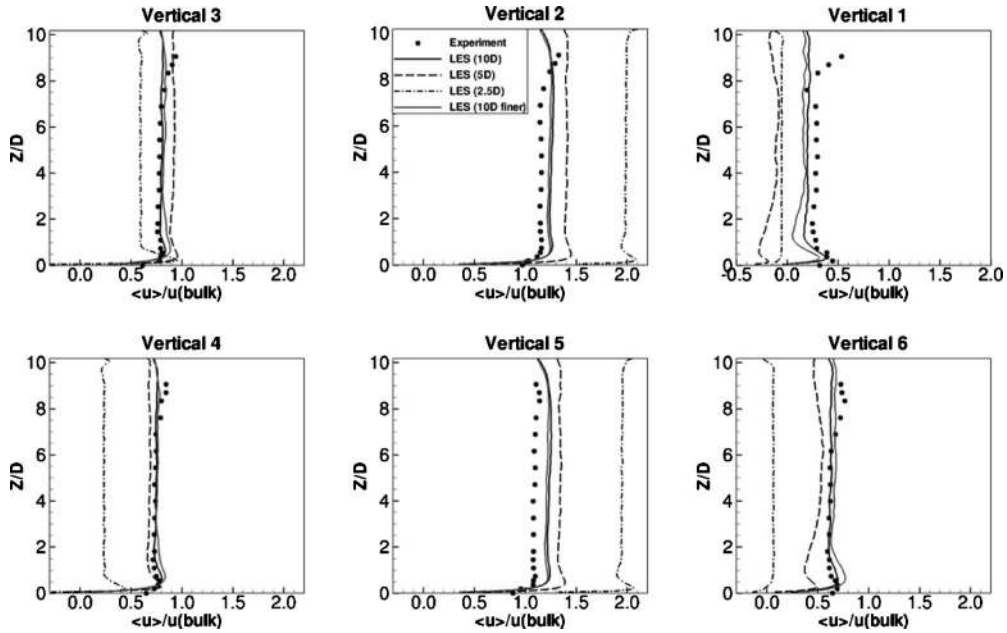

Fig. 4. Time-averaged streamwise velocity profile along the six selected verticals for the 10D, 5D, and 2.5D case at R_D=1,340

J. Hydraul. Eng. 2010.136:1003-1017.

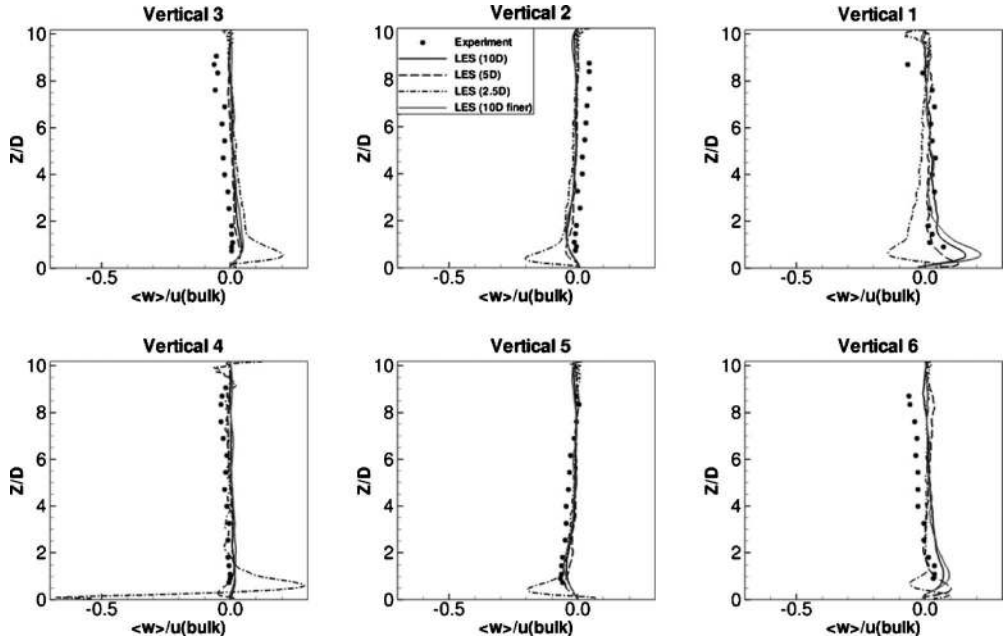

Fig. 5. Time-averaged vertical velocity profile along the six selected verticals for the 10D, 5D, and 2.5D case at R_D=1,340

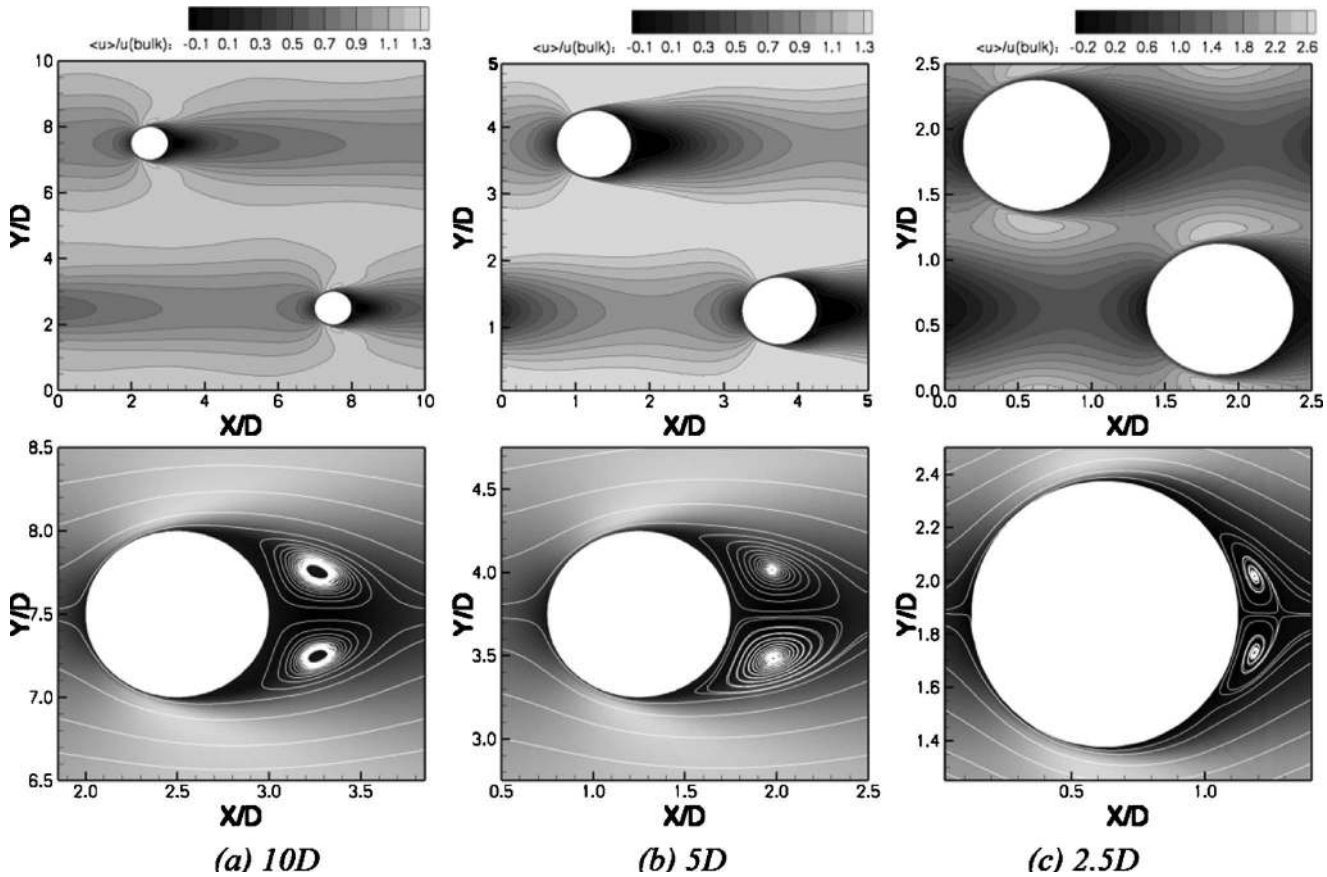

Fig. 6. Distribution of time-averaged streamwise velocities in a horizontal plane at Z/D=0.5 (upper row) and streamlines around the cylinder (lower row) for the three cases at R_D=1,340

J. Hydraul. Eng. 2010.136:1003-1017.

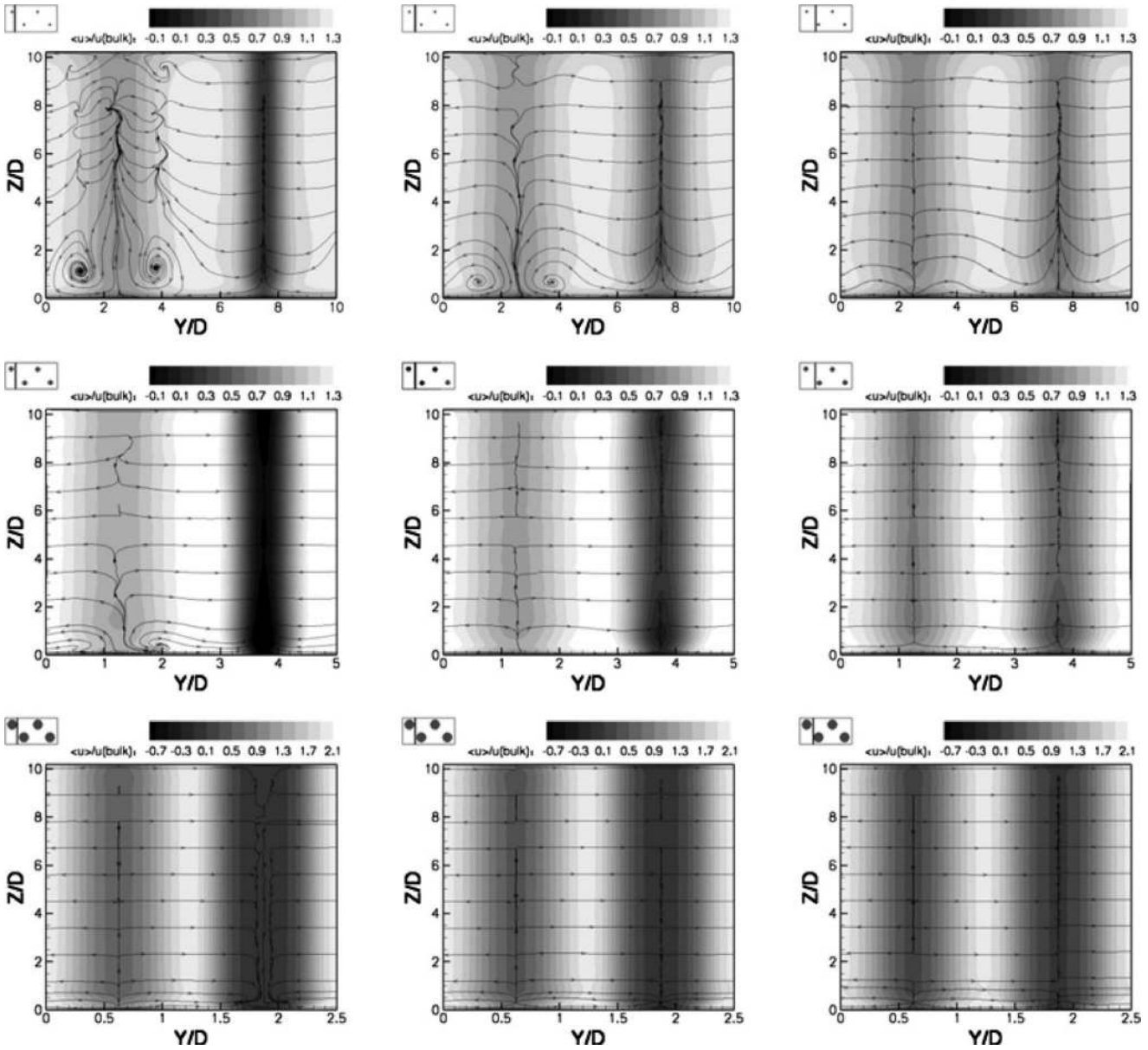

Fig. 7. Distribution of time-averaged streamwise velocity and streamlines of the secondary flow in three cross sections (the location is indicated in the sketch in the upper left of each figure and corresponds to $X/D=1s/4$, $X/D=2s/4$, $X/D=3s/4$) for the 10D (upper row), 5D (middle row), and 2.5D (lower row) cases at $R_D=1{,}340$

indicate considerable upward movement of fluid. In the 2.5D case, however, upward and downward movement of fluid is observed close to the bed in all verticals.

Fig. 6 presents contours of the time-averaged streamwise velocity and streamlines at about half depth for the three different vegetation densities investigated. While in the 10D and 5D cases a clear wake behind the cylinder and an area of higher velocities between the cylinders is identified, the 2.5D flow field exhibits large velocity gradients in both streamwise and spanwise directions. In the 10D and 5D cases, the maximum velocity is found to be about 30% higher than the bulk velocity, whereas in the 2.5D case the flow accelerates to about 2.5 times the bulk velocity between cylinders. The streamlines of the flow, presented in the lower half of the figure, reveal that the 10D and 5D cases exhibit similar flow features, i.e., flow separation at approximately *95°* and a relatively large recirculation region comprising two counterrotating vortices that are about the length of the cylinder diameter. In the 2.5D case the flow separates considerably later (at approximately 130°) and the recirculation region behind the cylinder in the 2.5D case is much smaller than the ones found behind the cylinders of the 10D and 5D case, respectively. The length of the vortex pair behind the 2.5D case cylinder is approximately only 1/4 of the cylinder diameter.

Fig. 7 presents contours of the primary flow velocity and streamlines of the secondary flow in three selected cross sections for the three vegetation densities. In the 10D case (upper row) a distinct secondary flow pattern develops behind the cylinder featuring a counterrotating vortex pair near the bed. This vortex pair is a result of fluid entrainment from the high momentum region between the cylinders filling the low momentum wake behind the cylinder. The fluid that enters the wake behind the cylinder from either side converges at the cylinder-axis, initiates an upflow (see also Profile #1 in Fig. 5) and results in the vortex pair. The vortex pair diminishes rather quickly. In the 5D case (middle row) a

J. Hydraul. Eng. 2010.136:1003-1017.

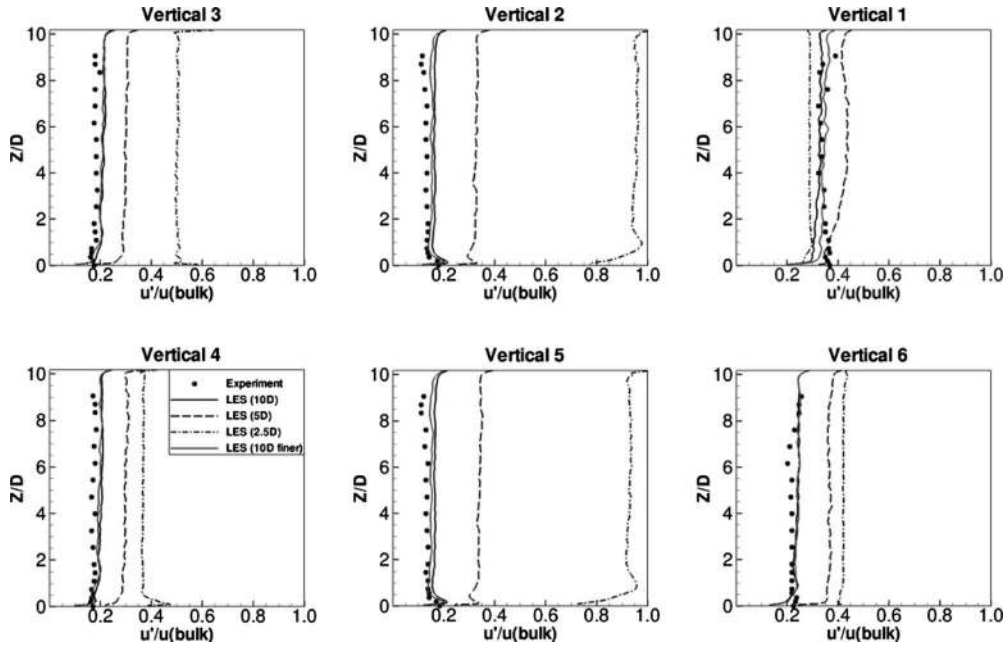

Fig. 8. Profiles of streamwise turbulence intensities of the LES along the six selected verticals for the 10*D*, 5*D*, and 2.5*D* case at R_D=1,340

similar counterrotating vortex pair is also being formed, however it appears to be flatter and less developed than in the 10*D* case. The distance behind the cylinder is too short for the vortices to fully develop. Also the upflow of fluid behind the cylinder is slightly weaker than in the 10*D* case (see also Profile #1 in Fig. 5). The 2.5*D* case does not exhibit a distinct secondary flow pattern, nevertheless strong vertical movement is observed but only very close to the bed (see also Fig. 5). Also interesting is the fact that behind the 2.5*D* cylinder downflow occurs whereas in the other two cases upflow is found.

The above discussed flow features are reflected in the turbulence intensity distribution along the six verticals. In Fig. 8 measured (for the 10*D* case from Liu et al. 2008) and computed streamwise turbulence intensities (i.e., the RMS of the velocity fluctuation normalized with the bulk velocity, u'/u(bulk)) are plotted. The comparison of computed streamwise turbulence intensities (solid line) with the measured values is very agreeable (regardless of grid resolution). The biggest differences are found near the bed in Vertical #1, which is the recirculation region with the highest turbulence, where the finer grid provides a better match, hence discrepancies in the original grid simulation can be attributed to the fact that only the resolved RMS quantities of the LES are plotted. The sreamwise turbulence intensity profiles are similar for all three cases and are almost a straight vertical line. This is significantly different from unobstructed channel flow not only in shape but also in magnitude. The 10*D* and the 5*D* cases

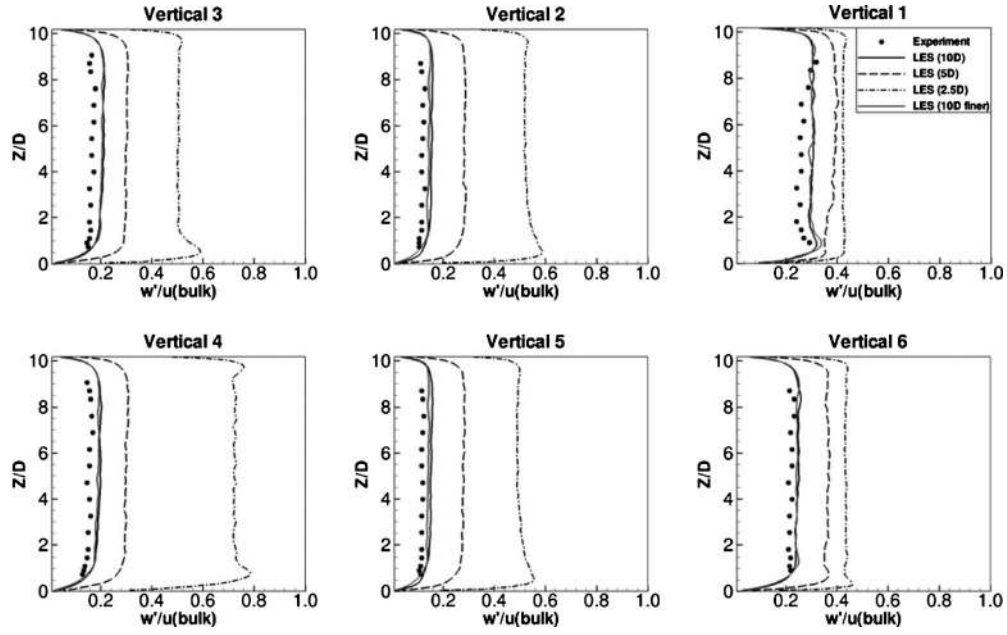

Fig. 9. Profiles of vertical turbulence intensities of the LES along the six selected verticals for the 10*D*, 5*D*, and 2.5*D* case at R_D=1,340

J. Hydraul. Eng. 2010.136:1003-1017.

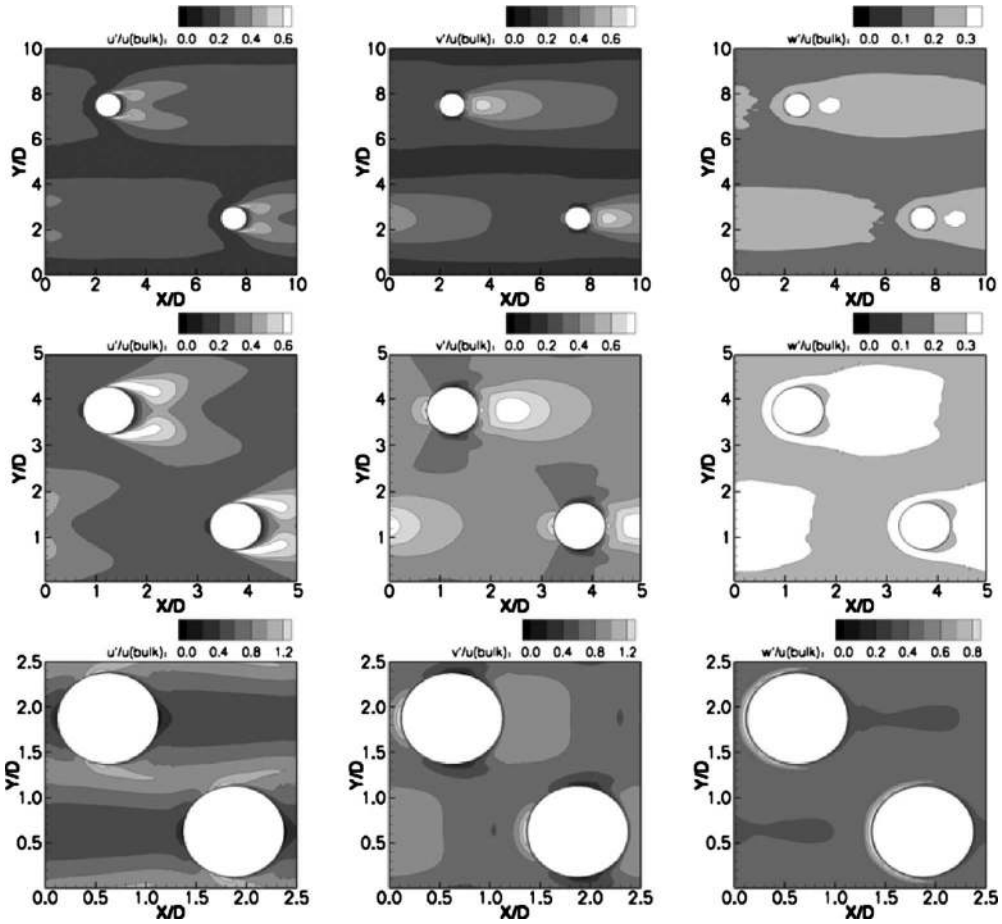

Fig. 10. Distribution of the three turbulence intensities [u'/u(bulk), left column, v'/u(bulk), middle column, w'/u(bulk, right column)] at one-half depth for the three vegetation densities (top row 10D, middle row 5D, lower row 2.5D)

exhibit the same behavior, however slightly higher streamwise turbulence intensities are observed in the 5D case. The 2.5D case exhibits considerably higher streamwise turbulence intensities, in particular between the cylinders (i.e., Verticals #2 and #5), which is a result of both spanwise and streamwise velocity gradients. The strong up and downflow close to the bed in the 2.5D case is reflected in kinks in the streamwise turbulence intensity profiles near the bed.

A quantitative comparison between measured (Liu et al. 2008) and computed normalized vertical turbulence intensities (for the 10D case) is provided in Fig. 9. Computed vertical turbulence intensities are in good agreement with the measurements for all six verticals. The distributions from the finer grid simulation are identical to the ones from the original grid. A small peak can be seen near the bed of Profile #1, a result of the relatively strong upward movement of fluid behind the cylinder. The 5D and the 2.5D distributions of vertical turbulence intensity are generally similar to the 10D case, but with higher magnitudes. There are peaks of vertical turbulence intensity near the bed in the 2.5D case, a result of the strong vertical movement.

Fig. 10 depicts turbulence intensities of the three components of the velocity vector in a horizontal plane at approximately half depth (Z=5D). While the 10D and 5D distributions of turbulence intensities are similar to each other, the 2.5D distributions are obviously different from the 10D and 5D cases. The most obvious difference is that the wake of the 10D and 5D case is characterized by high turbulence intensities while the wake of the 2.5D case has lower values of turbulence intensity. In the 10D case there is a corridor between cylinders, (i.e., around $Y/D=5$) which is characterized by very low values of turbulence intensities. This implies that the flow and turbulence downstream of the cylinder is not affected by the cylinders that are arranged laterally. In the 5D case, the distribution of turbulence intensities do not exhibit a distinct corridor with low values suggesting that the wake behind the cylinder is influenced by lateral cylinders. In the 2.5D case highest turbulence intensities are found in the area between the cylinders, being a result of local acceleration in the streamwise direction. In the 10D and 5D cases, streamwise turbulence intensities peaks are observed downstream of the flow separation from the cylinder, (i.e., 95°) resulting in a sickle shaped distribution of maximum turbulence intensities. The distributions look very similar to those of the flow around a long isolated cylinder. The streamwise turbulence intensity peaks in the 2.5D case occur clearly upstream of flow separation, which is where the maximum streamwise velocity is found (see also Fig. 6). Areas of high spanwise and vertical turbulence intensities are present in the vicinity of the stagnation point. This is due to vortices that are shed upstream impinging on the cylinder. In the 2.5D case the highest spanwise and vertical turbulence intensities occur upstream of the cylinder, while there is hardly any turbulence downstream of the cylinder. This is due to the fact that the 2.5D case does not exhibit distinct vortex shedding as in single cylinder flow. Clearly the

J. Hydraul. Eng. 2010.136:1003-1017.

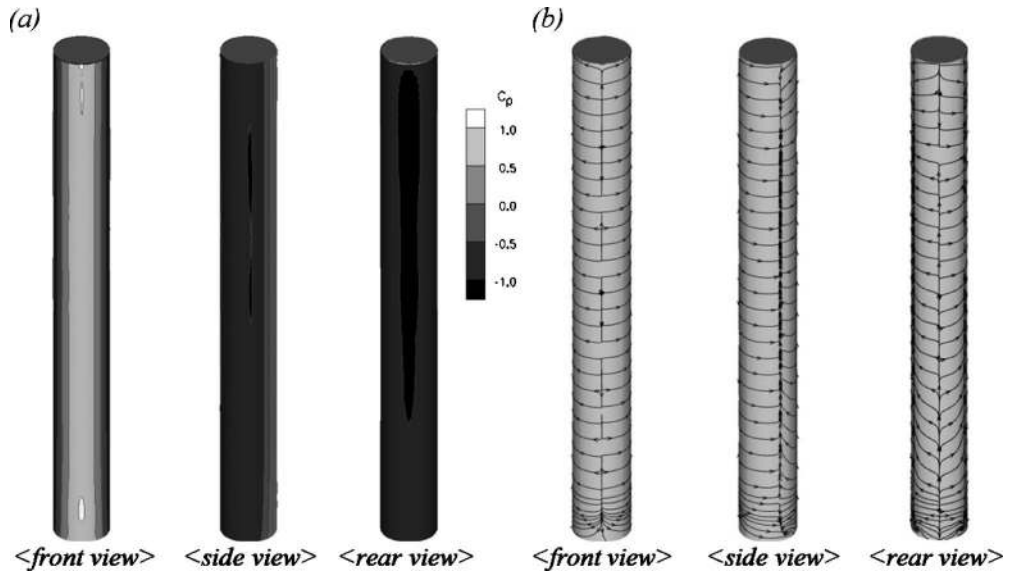

Fig. 11. (a) Pressure distribution; (b) streamlines on one cylinders of the 10*D* case

turbulence in the 2.5*D* case is rather generated by high streamwise velocity gradients, while von Karman vortex shedding occurs in the 5*D* and 10*D* cases.

Drag forces on the cylinder are a result of pressure differences between the upstream and downstream side of the cylinder and by viscous stresses on the cylinder. From the time-averaged velocity and pressure fields the drag force on the cylinder, decomposed into a pressure drag and a friction drag component, and the friction drag on the channel bed are calculated. Fig. 11(a) presents contours of the time-averaged pressure coefficient C_p on one cylinder of the 10*D* case from different perspectives (i.e., at the front view, side view and rear view). High C_p values are found in the vicinity of the stagnation point and the magnitude is almost constant over the entire cylinder height. Time-averaged flow separation occurs at approximately 95°, the location at which the coefficient of pressure turns negative due to the formation of the recirculation zone behind the cylinder. The negative pressure coefficient behind the cylinder is seen in the rear view, again showing almost constant C_p values over the entire depth. Streamlines on the 10*D* cylinder, viewed from three different perspectives, are provided in Fig. 11(b). The flow diverges at the stagnation point and the time-averaged flow appears to be two-dimensional except close to the bottom, where some downward movement is observed. The side view shows the separation line at a fairly constant angle of 95°. This line is therefore largely vertical and only at the bottom it is slightly bent in the downstream direction as the separation occurs a little later. In the rear region, the motion is primarily backward and upward along the cylinder as was discussed already. Near the bed there is only a backward component around the cylinder, which seems to be originating from a nodal point near the ground. This backward motion near the ground rolls up, as it approaches the slightly delayed separation point at the sidewall so that a focal point develops associated with a vortex. This vortex however is very close to the bed, is very weak and quickly disappears.

Fig. 12 presents the contributions of both pressure drag and friction drag on the cylinder as well as the integral force from the bed shear stresses to the total flow resistance in channel flow through vegetation for the three vegetation densities and the two cylinder Reynolds numbers R_D. Clearly, flow resistance is mainly due to the presence of the cylinder. For the higher renumber cases pressure drag accounts for approximately 90%, friction drag for approximately 6–7% and the bed shear stress decreases with increasing vegetation density and is almost negligible, especially in

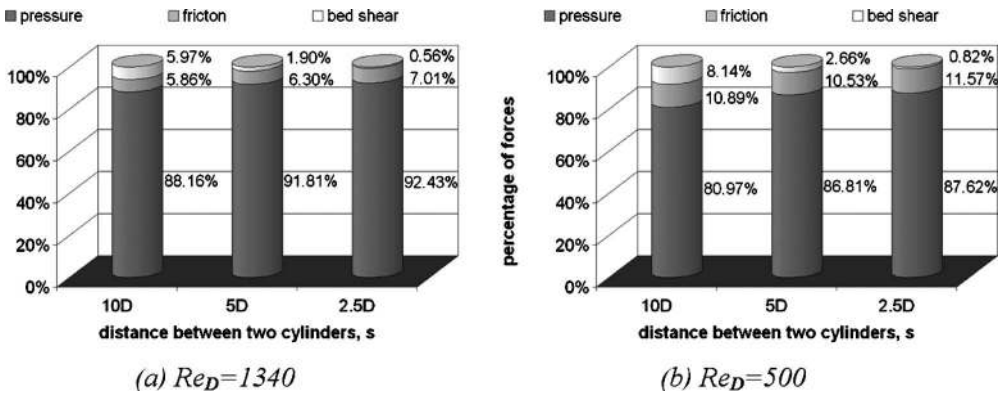

Fig. 12. Contributions of pressure drag, friction drag, and bed shear to the total energy loss in flow through vegetation at various vegetation density and Reynolds numbers

J. Hydraul. Eng. 2010.136:1003-1017.

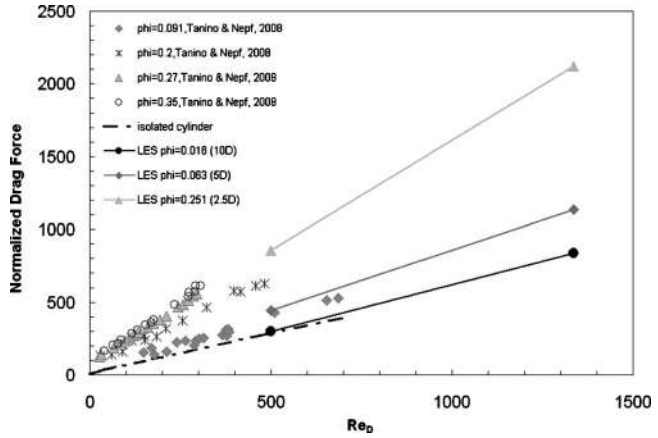

Fig. 13. Normalized drag force as a function of cylinder Reynolds number for various vegetation densities

the 2.5*D* case. The vegetation density has almost no effect on the percentage distribution of the contributing forces to the overall loss. For the lower R_D cases shear forces are slightly increased however, pressure drag still accounts for about 80–90% of the total loss. The portion of friction drag is constant regardless of vegetation density and the contribution of bed shear stress decreases with an increase in vegetation density.

The normalized drag force, defined as $F_D = f_D/(\mu u(\text{bulk})h)$, on the cylinder is compared with measured normalized drag forces of flow through emergent vegetation from a recent experimental study (Tanino and Nepf 2008). Tanino and Nepf (2008) carried out laboratory experiments to investigate the effect of cylinder Reynolds number and vegetation density (characterized by the solid volume fraction, $\varphi = m\pi D^2/4$, in which m = number of cylinders per unit horizontal area) on the drag force and on the drag coefficient. Tanino and Nepf (2008) covered a fairly wide range

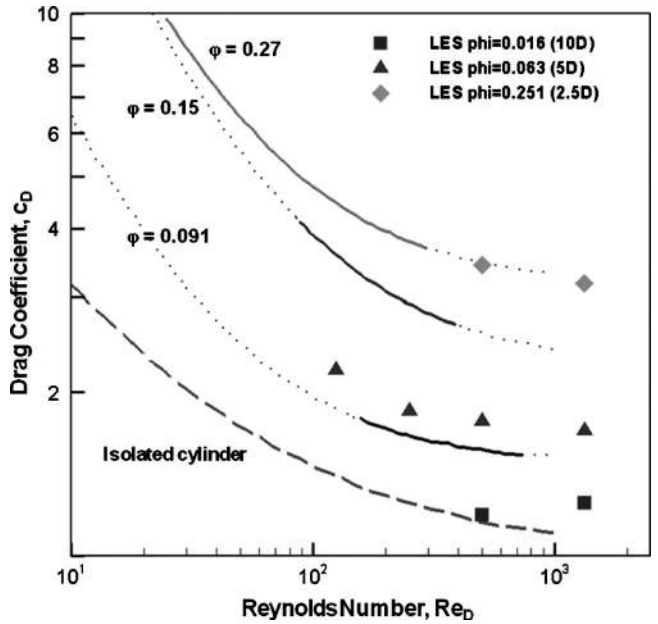

Fig. 14. Drag coefficient c_D as a function of cylinder Reynolds number for various vegetation densities (lines represent experimental data from Tanino and Nepf 2008)

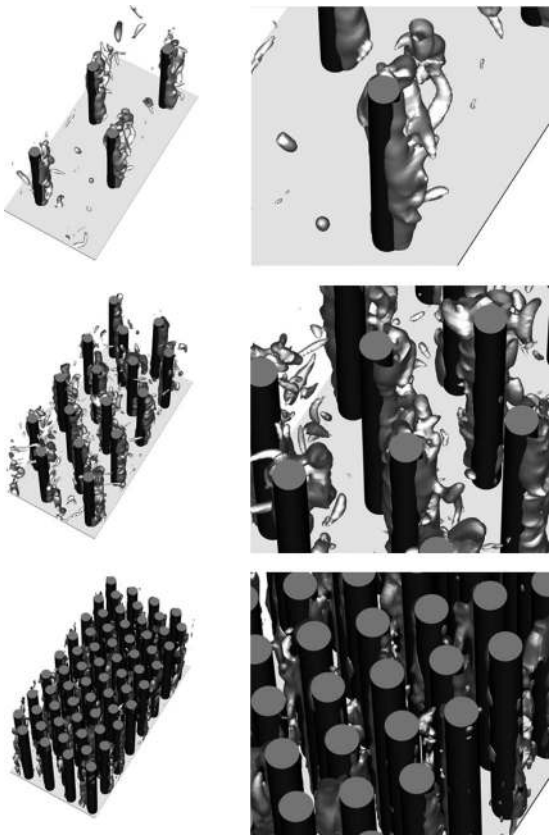

Fig. 15. Isosurfaces of pressure fluctuations for the three vegetation densities (10*D*, upper row; 5*D*, middle row; 2.5*D*, lower row)

of vegetation densities, i.e., $0.091 < \varphi < 0.35$. The LES presented herein have a vegetation density of $\varphi = 0.016$, 0.063, and 0.251, for the 10*D*, 5*D*, and 2.5*D* case, respectively.

The LES calculated drag forces as a function of cylinder Reynolds number are plotted together with Tanino and Nepf's measured values in Fig. 13. The LES complement nicely the previous experimental observations and match the observed trends remarkably well. This is particularly obvious for the 2.5*D* case (with $\varphi = 0.25$) for which the LES computed drag force can be regarded as a direct extension to the measured drag forces from the experiment with almost the same density of $\varphi = 0.27$. The drag force distribution of the 10*D* case exhibits the same behavior as an isolated cylinder (dashed line, White 1991) suggesting that the flow recovers sufficiently behind each cylinder. With an increase in both the vegetation density and the cylinder Reynolds number the drag force increases.

Drag coefficients are calculated and are compared with the values obtained by Tanino and Nepf (2008) in Fig. 14. The calculated drag coefficients c_D show a reasonable match with the extrapolated line from the experimental data. The drag coefficient is clearly a function of the cylinder Reynolds number, at least for lower values of R_D. A greater influence on the value of c_D is the vegetation density, and it seems that the increase is linear, i.e., as the vegetation density doubles, the value of the drag coefficient doubles.

Instantaneous Flow Field and Turbulence Structures

An impression of the development of large-scale vortical structures can be obtained from the temporal development of isosur-

J. Hydraul. Eng. 2010.136:1003-1017.

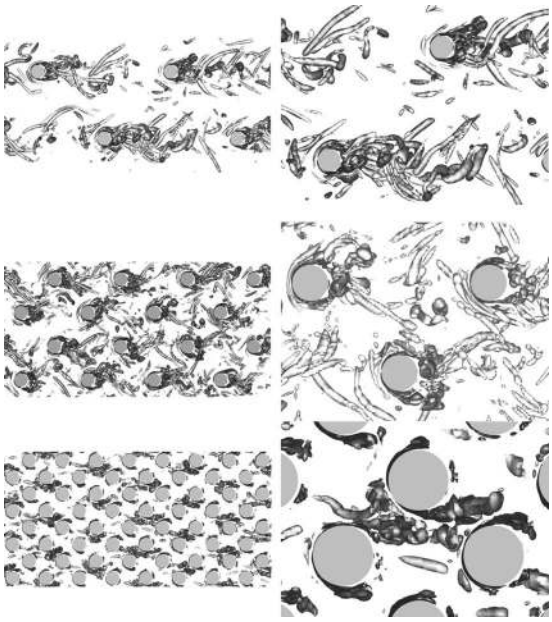

Fig. 16. Instantaneous isosurfaces of the Q-criterion for the three vegetation densities (10D, upper row; 5D, middle row; 2.5D, lower row)

faces of the pressure perturbation $p' = (p - \langle p \rangle)/(\rho U_\infty^2)$. Snapshots showing such isosurfaces in an oblique view are presented in Fig. 15. For both the 10D and 5D cases vortices are observed shedding from the cylinder due to Kelvin Helmholtz instability. These vortices extend over the full cylinder height, display clear two dimensionality and are similar than von Karman vortices behind long isolated cylinders. In the 2.5D case the process is influenced strongly by the above discussed flow acceleration between cylinders and the prevailing high levels of turbulence, which alter the shedding process. As a result, these vortices are less coherent and do not exhibit clear two dimensionality.

Snapshots of three-dimensional turbulence structures visualized with isosurfaces of the Q-criterion (Hunt et al. 1988) for the three vegetation densities are presented in Fig. 16. In the 10D case (upper row) the above mentioned von Karman-type vortices are clearly visible. While these structures exhibit two dimensionality in their early stage, they are stretched in the streamwise direction and packets of smaller vortices evolve, which eventually impinge on the downstream cylinder. In the above mentioned corridor between cylinders there are hardly any vortices present supporting the above made statements that the flow behind the cylinder is not interfered with structures from lateral cylinders. In the blow-up on the right hand side of Fig. 16(a) the occurrence of alternating vortex shedding is indicated by the black lines. In Fig. 16(a), alternating shedding is observed, the vortices on opposite sides being offset and the distance between vortices on the same side being rather large. In the 5D case, depicted in Fig. 16(b), the vortex shedding from the cylinder walls is influenced by vortices shed from upstream and lateral cylinders. The quasi-two-dimensional structure of the von Karman vortices is apparent close to the cylinder. In contrast to the 10D case, these vortices remain rather strong when they impinge on the downstream cylinder, with the consequence that they alter the shedding behavior of the vortices there. Also vortices from lateral cylinders seem to be entering the wake behind the cylinder. These flow features are reflected in the shedding behavior and while in the 10D case only regular, alternating shedding is observed, shedding in the 5D case becomes more irregular. Both alternating vortex shedding (A-B-C) as well as symmetric shedding (D-E), i.e., the vortices on opposite sides show little longitudinal offset, is seen. The vortex interference is amplified in the 2.5D case [Fig. 16(c)] and vortex shedding occurs irregularly. In the blow-up on the right hand side of Fig. 16(c) both alternating (A-B) and symmetric (D-E) shedding is observed. The frequency of vortex shedding is visibly increased, i.e., the longitudinal distance between vortex cores is much shorter in the 2.5D case than in the 10D and 5D cases. Animations of the 2.5D case have shown that some vortices impinge on the cylinder located immediately downstream while others are convected through the gaps and impinge on a lateral cylinder further downstream. Also, these vortices maintain their strength over a considerable distance. These animations can be accessed at http://cfd.ce.gatech.edu/index_files/ASCEvegetation.htm.

The horizontal distribution of vertical vorticity (z-vorticity) at an instant in time and in a plane approximately at one-half water depth (Z=5D) for the three vegetation densities is presented in Fig. 17. The findings from the analysis of Figs. 15 and 16 are confirmed by the contours of vertical vorticity. In the 10D case, strong two-dimensionality of the von Karman vortices close to the cylinder is indicated with high levels of vertical vorticity, decreasing while the vortices are being convected downstream. In the vicinity of the downstream cylinder z-vorticity magnitudes are close to zero. Regular alternating shedding of clockwise and counterclockwise rotating vortices occurs. As the density of vegetation increases, the vortex shedding at the cylinders is influenced by vortices that are shed from upstream cylinders resulting

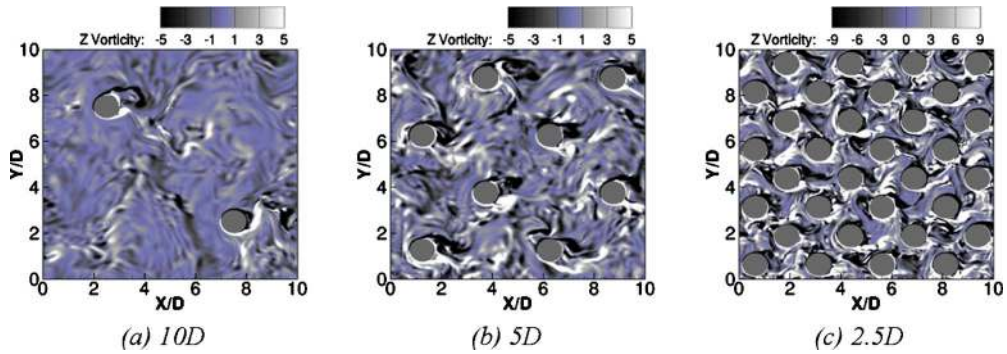

Fig. 17. Contours of instantaneous vorticity in a horizontal plane at half channel depth for the three vegetation densities (note that the 2.5D case has a different scale)

J. Hydraul. Eng. 2010.136:1003-1017.

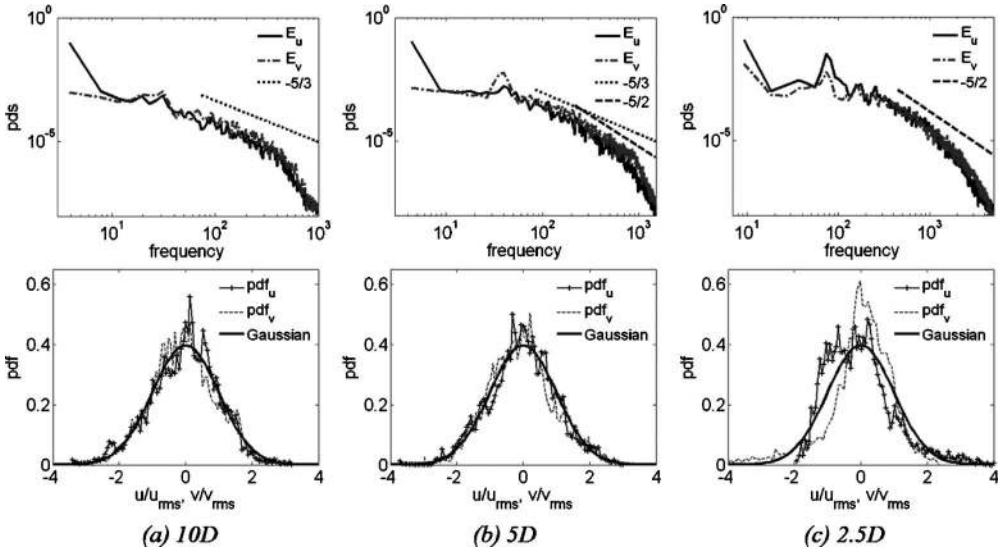

Fig. 18. Time signals of the streamwise and spanwise velocity component (upper row), velocity spectra (middle row), and normalized PDF (lower row) at a location (half depth) along vertical 2

in a more irregular shedding behavior. This is supported by elevated levels of vertical vorticity in front of cylinders in the 5*D* case. The magnitude of vertical vorticity in the 5*D* case is similar to the 10*D* case. A further increase in vegetation density results in an increase in vorticity magnitude with the magnitude of vertical vorticity levels being almost twice as high in the 2.5*D* case as in the 10*D* or 5*D* case, respectively.

Time signals of all three velocity components were recorded at selected points over a duration of 0.5 (for the 2.5*D* case) to 1.0 (for the 10*D* case) in dimensionless eddy turn over time units $t_e = H/u_*$ by storing every 10th point in time. Spectra of the streamwise and spanwise components obtained with the method of Welch (Press et al. 1992) are reported here as they best reveal the presence of von Karman vortex shedding. Also probability density functions (PDF) of the time signal were obtained to further analyze the instantaneous flow field. Spectra in the cylinder wake at approximately half depth are depicted in the upper row of Fig. 18 for the three vegetation densities. The vortex shedding frequency is identified as a distinct peak in the velocity spectra, in particular the one of the spanwise velocity component. For the 10*D* case the peak occurs at approximately $f=30$ Hz corresponding to a Strouhal number of $\mathrm{S}=fD/u(\mathrm{bulk})=0.197$ while for the 5*D* case a slightly higher shedding frequency ($f=32$ Hz) is obtained from the peak in the spectra and corresponds to a Strouhal number of $\mathrm{S}=0.21$. For the 2.5*D* case however, vortex shedding occurs at a much higher frequency, in fact almost three times as high as the other two cases ($f=90$ Hz). This corresponds to a Strouhal number of $\mathrm{S}=0.5$. Furthermore, the spectra of the 10*D* case and in large parts of the 5*D* case exhibit a pronounced $-5/3$ (dotted line) decay of energy as typically observed in wake flows with alternating vortex shedding. The velocity spectrum for the 5*D* case arguably exhibits two different slopes in the inertial range as is notable when comparing to the two straight lines representing the $-5/3$ slope (dotted line) and a $-5/2$ slope (dashed line). It seems that at higher frequencies energy transfer to smaller scales is accomplished at higher rates, suggesting vortex interference. Rather interesting is the velocity spectrum of the 2.5*D* case: vortex interference is clearly visible as the spectrum exhibits multiple peaks, i.e., vortices that are shed at upstream cylinders and entering the wake of the present cylinder. This is in good qualitative agreement with Umeda and Yang (1999) who investigated vortex shedding in dense tube bundles. The two additional peaks have similar levels of energy than the primary peak and reflect additional vortices shed from an upstream cylinder and a cylinder located laterally. Also, noteworthy is the fact that the inertial subrange (here covered over a frequency decade) in the 2.5*D* case does not exhibit the classical $-5/3$ Kolmogorov subrange but rather follows a steeper $-5/2$ energy transfer range. This is the result of strong streamwise and spanwise velocity gradients with the vortex being confinement and accelerated between cylinders. This obviously results in faster energy transfer from large-scales to small scales. For all three cases the range in frequency between the shedding mode(s) and the high-frequency mode with larger slope, at which energy is rapidly dissipated via SGS modeling, spans more than a decade. In amplitude the range is almost two decades. Both ranges covered by the LES demonstrate the good spatial and temporal resolution of the simulations.

The normalized PDF of the streamwise and vertical velocity signals of the 10*D* and 5*D* cases show a similar behavior and appear to be distributed normally. Fairly significant differences are observed in PDF of the 2.5*D* case for both streamwise and spanwise velocity signal. Both functions differ from a Gaussian distribution (solid line). The v-function has a pronounced peak around the zero value and seems to be skewed toward positive values but the signals are quite noisy and longer time-series is needed to provide conclusive evidence. The u-velocity function exhibits a multimodal behavior, a result of periodically passing through of vortices passing through the close spacing between cylinders.

Normalized (with the total drag) drag and lift forces on one cylinder over several eddy turn over time periods for the three cases and the two Reynolds numbers are plotted in Fig. 19. The drag and lift forces on the cylinder are due to vortex shedding and the shedding frequency is represented in the peaks of the drag force and well pronounced in the positive and negative peak values of the lift force. The smaller amplitude of the lift force at some instants in time in the 10*D* and 5*D* cases can be attributed to upstream turbulence. The severe vortex interaction in the 2.5*D* case is visible in the distribution of the lift force over time as the line is not as smooth as in the other cases showing the aforemen-

J. Hydraul. Eng. 2010.136:1003-1017.

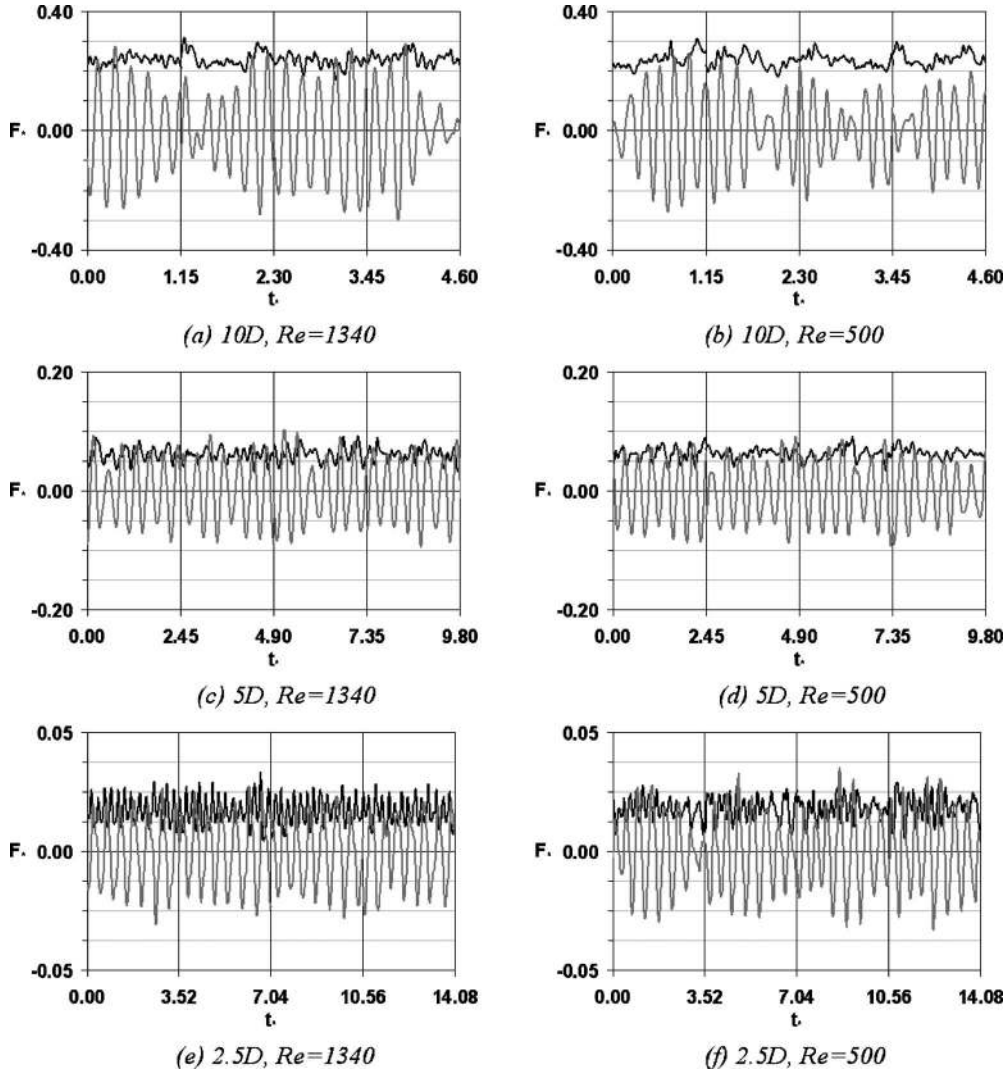

Fig. 19. Temporal distribution of lift (gray line) and drag (black line) forces for the three vegetation densities and the two R numbers

tioned high-frequency fluctuations. For the lower cylinder Reynolds number, the shedding frequencies are almost identical for the 10*D* and 5*D* cases while with an increase in viscous effects, the shedding frequency is decreased in the 2.5*D* case leading to a lower Strouhal numbers of S=0.5 for the R_D=500 case.

The Strouhal numbers of the six simulations performed in this study are plotted in Fig. 20 together with values from previous studies. All observations made above suggest that the 10*D* case exhibits features that are very similar to single cylinder flow and this is also confirmed by the comparison of the S number as a function of R_D. The values obtained herein match rather well the isolated cylinder values of Zhang and Dalton (1997), Kevlahan (2007) or Liu and Fu (2003) or the theoretical curve provided by Norberg (2003) which is a result of an extensive literature review on flow around isolated cylinders. For the cylinder, Reynolds numbers covered herein, the Strouhal number in the flow through vegetation appears to be independent of R_D a finding that is in line with observations made for isolated cylinders. As the density increases there is an increase in Strouhal number but again no obvious dependency on the cylinder Reynolds number. Comparison with the experiments of flow through a staggered array of cylinders (also at a density of 5*D*) confirms this finding. The Strouhal numbers obtained in this study match the ones found by

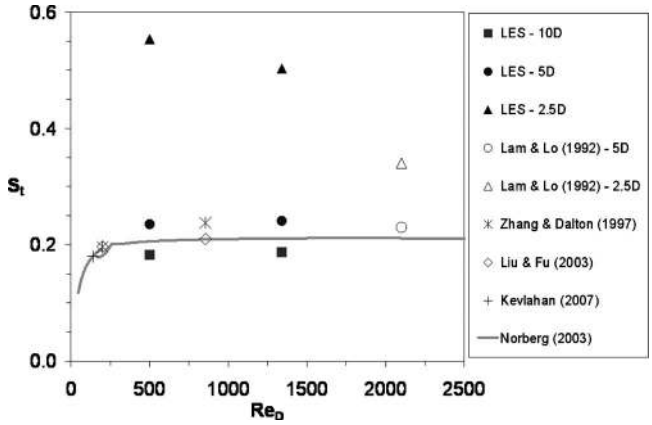

Fig. 20. Strouhal number as a function of cylinder Reynolds number for the LES performed in this study versus isolated cylinder and tube bundle flow

J. Hydraul. Eng. 2010.136:1003-1017.

Lam and Lo (1992) pretty well. The distribution of the Strouhal number as a function of R_D for the 2.5D case however suggests that there is a dependency of S on the cylinder Reynolds number at higher vegetation densities as the Strouhal numbers decrease with an increase in R_D. This is again in agreement with the observations of Lam and Lo (1992).

Conclusions

Several large-eddy simulations of flow through a matrix of regularly arranged emergent cylinder were performed. For a low vegetation density, experimental data obtained from Liu et al. (2008) were used to validate the first LES. Good agreement was found between measured and simulated data confirming the great accuracy of the LES method. Further simulations at higher vegetation density and at a second, lower cylinder Reynolds number were carried out to study the effect of vegetation density and cylinder Reynolds number on the mean flow, the turbulence statistics, flow resistance and instantaneous flow field. At low vegetation density, the flow behaves similar to the flow around an isolated cylinder, while there are significant structural differences at high cylinder density, which is reflected in the turbulence statistics as well as in the flow resistance. Calculated drag forces are in good agreement with experimental data and suggest that flow resistance increase with both density and cylinder Reynolds number. Visualized turbulence structures, velocity signal analysis, as well as distributions of the drag and lift force over time confirm the structural changes in the flow.

Notation

The following symbols are used in this paper:

C_s = Smagorinsky constant;
c_D = drag force coefficient;
D = cylinder diameter;
f = frequency;
h = water depth;
k_r = residual kinetic energy;
m = number of cylinders per unit horizontal area;
p = filtered pressure;
p' = pressure perturbation;
$\langle p \rangle$ = time-averaged pressure;
R = Reynolds number based on water depth;
R_D = Reynolds number based on cylinder diameter;
S_{ij} = filtered strain-rate tensor;
$|S|$ = characteristic filtered strain rate;
s = distance between two cylinders in same direction;
t = time;
t_e = eddy turn-over time;
U_∞ = free stream velocity
u = instantaneous velocity component in x direction;
u(bulk) = bulk velocity in x direction;
u_i and u_j = instantaneous velocity vector;
v = instantaneous velocity component in y direction;
w = instantaneous velocity component in z direction;
x = spatial position in x direction;
x_i = spatial position vector;
y = spatial position in y direction;
y^+ = boundary condition evaluation factor;
z = spatial position in z direction;
Δ = anisotropic characteristic filter size;
Δx = characteristic filter width in x direction;
Δy = characteristic filter width in y direction;
Δz = characteristic filter width in z direction;
δ_{ij} = kroneker delta;
ν_t = subgrid scale eddy viscosity;
ρ = fluid density;
τ_{ij} = stress tensor;
τ_{ij}^a = anisotropic stress tensor;
τ_w = wall shear stress;
φ = vegetation density; cylinder volume fraction;
ψ = width fraction factor; and
π = mathematical constant approximately equal to 3.14159.

References

Bennett, S. J., Pirim, T., and Barkdoll, B. D. (2002). "Using simulated emergent vegetation to alter stream flow direction within a straight experimental channel." *Geomorphology*, 44(1–2), 115–126.

Choi, S. U., and Kang, H. (2004). "Reynolds stress modeling of vegetated open channel flows." *J. Hydraul. Res.*, 42(1), 3–11.

Cui, J., and Neary, V. S. (2002). "Large-eddy simulation (LES) of fully developed flow through vegetation." *IAHR's 5th Int. Conf. on Hydroinformatics*.

Dunn, C. J., López, F., and García, M. H. (1996). "Mean flow and turbulence in a laboratory channel with simulated vegetation." *Hydraul. Engr. Series No. 51, UILU-ENG-96–2009*, UIUC, Ill.

Fischer-Antze, T., Stoesser, T., Bates, P. B., and Olsen, N. R. (2001). "3D numerical modelling of open-channel flow with submerged vegetation." *IAHR J. Hydraul. Res.*, 39, 303–310.

Germano, M., Piomelli, U., Moint, P., and Gebot, W. (1991). "A dynamic subgrid-scale eddy viscosity model." *Physics of Fluids, No.*, 3(7), 1760–1765.

Hanjalic, K., and Hadzic, I. (1998). "Third ERCOFTAC/IAHR workshop on refined flow modelling: Turbulent flow and heat transfer in a subchannel of a staggered tube bundle." *T.U. Delft Technical Report*, TU, Deft, Delft, The Netherlands.

Hunt, J. C. R., Wray, A. A., and Moin, P. (1988). "Eddies, stream, and convergence zones in turbulent flows." *Center for Turbulence Research Rep. No. CTR-S88*, Stanford Univ., Stanford, Calif.

Kevlahan, N. K. R. (2007). "Three-dimensional Floquet stability analysis of the wake in cylinder arrays." *J. Fluid Mech.*, 592, 79–88.

Lam, K., and Lo, S. C. (1992). "A visualization study of cross-flow around four cylinders in a square configuration." *J. Fluids Struct.*, 6, 109–131.

Lee, J. K., Roig, L. C., Jenter, H. L., and Visser, H. M. (2004). "Drag coefficients for modeling flow through emergent vegetation in the Florida Everglades." *Ecol. Eng.*, 22(4–5), 237–248.

Liu, D., Diplas, P., Fairbanks, J. D., and Hodges, C. C. (2008). "An experimental study of flow through rigid vegetation." *J. Geophys. Res.*, 113, F04015.

Liu, S., and Fu, S. (2003). "Regimes of vortex shedding from an in-line oscillating circular cylinder in the uniform flow." *Acta Mech.*, 19(2), 118–126.

Lopez, F., and Garcia, M. (2001). "Mean flow and turbulence structure of open-channel flow through non-emergent vegetation." *J. Hydraul. Eng.*, 127(5), 392–402.

Luebcke, H., Schmidt, S., Rung, T., and Thiele, F. (2001). "Comparison of LES and RANS in bluff body flows." *J. Wind. Eng. Ind. Aerodyn.*, 89, 1471–1485.

Naot, D., Nezu, I., and Nakagawa, H. (1996). "Hydrodynamic Behavior of partly vegetated open-channels." *J. Hydraul. Eng.*, 122(11), 625–633.

Neary, V. S. (2000). "Numerical model for open channel flow with vegetative resistance." *IAHR's 4th Int. Conf. on Hydroinformatics*.

J. Hydraul. Eng. 2010.136:1003-1017.

Nepf, H. M. (1999). "Drag, turbulence, and diffusion in flow through emergent vegetation." *Water Resour. Res.*, 35(2), 479–489.
Norberg, C. (2003). "Fluctuating lift on a circular cylinder: Review and new measurements." *J. Fluids Struct.*, 17, 57–96.
Palau, G. P., Stoesser, T., Rummel, A., and Rodi, W. (2007). "Turbulent shallow flow through emergent vegetation." *ICEH: Int. Conf. on Eco-hydraulics*.
Pasche, E., and Rouve, G. (1985). "Overbank flow with vegetatively roughened flood plains." *J. Hydr. Engrg.*, 111, 1262–1278.
Petryk, S., and Bosmajian, G., III. (1975). "Analysis of flow through vegetation." *J. Hydr. Div.*, 101(7), 871–884.
Pope, S. B. (2000). *Turbulent flows*, Cambridge University Press, Cambridge, U.K.
Press, W., Teukolsky, S., Vetterling, W., and Flannery, B. (1992) *Numerical recipes*, Cambridge, U.K.
Rodi, W. (1997). "Comparison of LES and RANS calculations of the flow around bluff bodies." *J. Wind Eng. Ind. Aerodyn.*, 69-71, 55–75.
Rollet-Miet, P., Laurence, D., and Ferziger, J. (1999). "LES and RANS of turbulent flow in tube bundles." *Int. J. Heat Fluid Flow*, 20, 241–254.
Shimizu, Y., and Tsujimoto, T. (1994). "Numerical analysis of turbulent open-channel flow over vegetation layer using a k-eps turbulence model." *J. Hydrosci. Hydr. Eng.*, 11(2), 57–67.
Smagorinsky, J. (1963). "General Circulation Experiments with the Primitive Equations." *Mon. Weather Rev.*, 91(3), 99–164.
Stoesser, T. (2002). "Development and validation of a CFD code for open-channel flows." Ph.D. thesis, Dept. of Civil Engineering, Univ. of Bristol, U.K.
Stoesser, T., Liang, C., Rodi, W., Jirka, G.H. (2006). "Large-eddy simulation of fully-developed turbulent flow through submerged vegetation." *Proc., Riverflow 2006*.
Stone, B. M., and Shen, H. T. (2002). "Hydraulic resistance of flow in channels with cylindrical roughness." *J. Hydr. Eng.*, 128(5), 500–506.
Takemura, T., and Tanaka, N. (2007). "Flow structures and drag characteristics of a colony-type emergent roughness model mounted on a flat plate in uniform flow." *Fluid Dyn. Res.*, 39(9–10), 694–710.
Tanino, Y., and Nepf, H. M. (2008). "Laboratory investigation of mean drag in a random array of rigid, emergent cylinders." *J. Hydr. Eng.*, 134(1), 34.
Tsihrintzis, V. A. (2001). "Discussion of Wu et al. 1999." *J. Hydr. Eng.*, 127(3), 241–244.
Tsujimoto, T., Kitamura, T. (1990). "Velocity profile of flow in vegetated-bed channels." *KHL Progressive Report, 1990*, Kanazawa Univ., Kanazawa, Japan.
Umeda, S., and Yang, W. J. (1999). "Interaction of von Karman vortices and intersecting main streams in staggered tube bundles." *Exp. Fluids*, 26, 389–396.
White, F. M. (1991). *Viscous fluid flow*, 2nd Ed., McGraw-Hill, New York.
Wilson, C. A. M. E., Stoesser, T., Bates, P. D., and Batemann Pinzen, A. (2003). "Open channel flow through different forms of submerged flexible vegetation." *J. Hydraul. Eng.*, 129, 847–853.
Wu, F. C., Shen, H. W., and Chou, Y. J. (1999). "Variation of Roughness coefficients for unsubmerged and submerged vegetation." *J. Hydr. Eng.*, 125, 934.
Zhang, J. F., and Dalton, C. (1997). "Interaction of a steady approach flow and a circular cylinder undergoing forced oscillation." *ASME J. Fluids Eng.*, 119, 802–813.

J. Hydraul. Eng. 2010.136:1003-1017.